Geochemistry, Geophysics, Geosystems

Supporting Information for

Heralds of a future volcanism: Swarms of microseismicity beneath the submarine Kolumbo volcano indicate opening of near-vertical fractures exploited by ascending melts

F. Schmid[1,*], G. Petersen[2,3], E. Hooft[4], M. Paulatto[5], K. Chrapkiewicz[5], M. Hensch[6], T. Dahm[2,7]

Affiliations:

[1]GEOMAR Helmholtz-Centre for Ocean Research Kiel, German

[2]University of Utah Seismograph Stations, University of Utah, Salt Lake City, Utah, U.S.A.

[3]GFZ Helmholtz-Centre Potsdam, German Research Centre for Geosciences Potsdam, Germany

[4]University of Oregon, Eugene, USA

[5]Imperial College London, Department of Earth Science and Engineering, Prince Consort Road, UK

[6]Geological Survey, of Baden-Württemberg, Freiburg, Germany

[7]University of Potsdam, Germany

*Now at K.U.M. Umwelt und Meerestechnik Kiel GmbH, Germany

Contents of this file

Introduction

This file contains additional figures that are helpful to understand the dataset and results presented in the related manuscript.

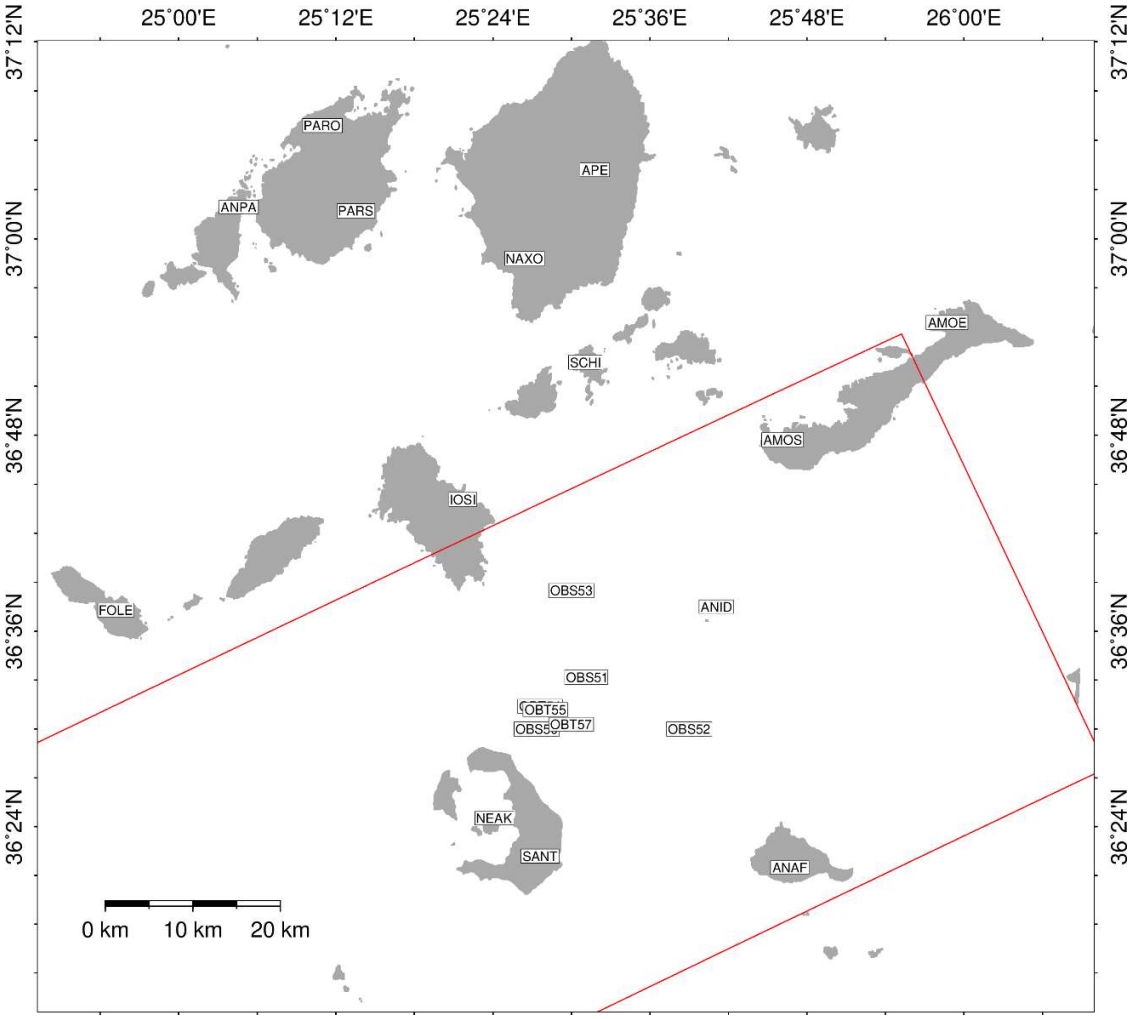

Figure S1. Full extent of the seismological network (including land stations and ocean bottom stations) that operated between June 2006 till March 2007 and recorded phase arrival information used in the earthquake location process. Labels give station names and gray shading outlines Cycladic islands. The red square indicates the extent of the 3D Vp-model from Hooft et al., 2019 which was used in the earthquake location process. Beyond the red square the 3D Vp-model was extrapolated to fill the entire map area.

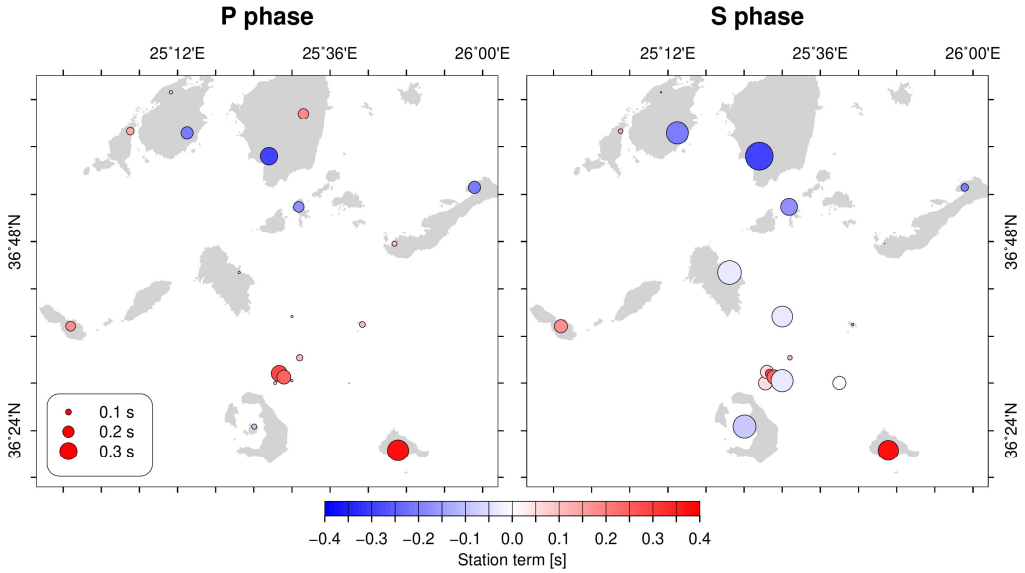

Figure S2. Graphical representation of station correction terms for individual stations in the network, determined by iteratively locating the hypocentres with NonLinLoc software. Colours represent the sign and size the magnitude of the station correction terms.

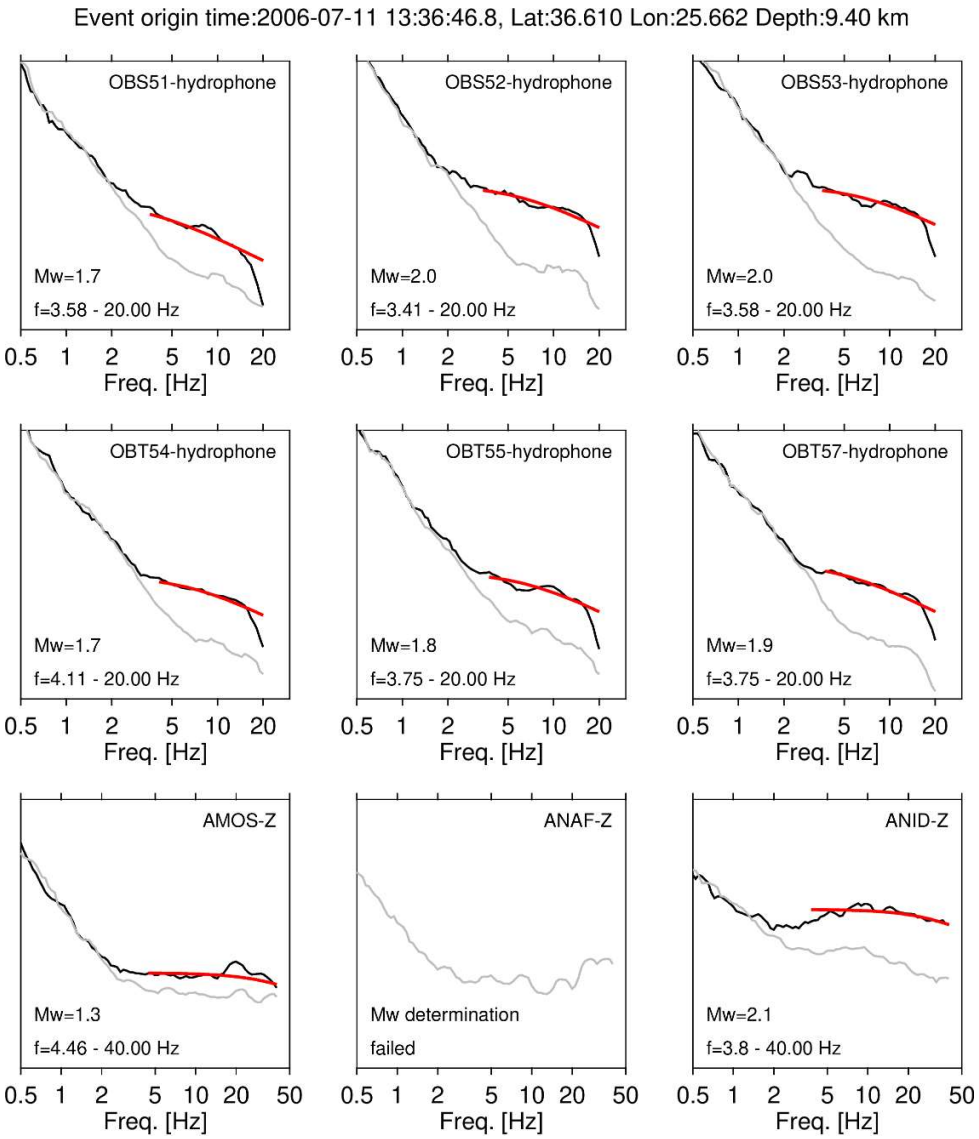

Figure S3. Plot of spectral fits during Mw magnitude determination for an exemplary earthquake (source parameter are printed near top). Black curves show the signal spectrum. Gray curves show the noise spectrum determined for the 30 second period prior to the first arrival. Red curves show the best-fitting synthetic spectrum. Station and used channel are provided in the top right corner. Determined Mw magnitude and frequency ranged used for fitting are given near the lower left corner. Amplitude is in arbitrary units. Please note that ocean bottom station data have a sampling rate of 50 Hz and land station data 100 Hz.

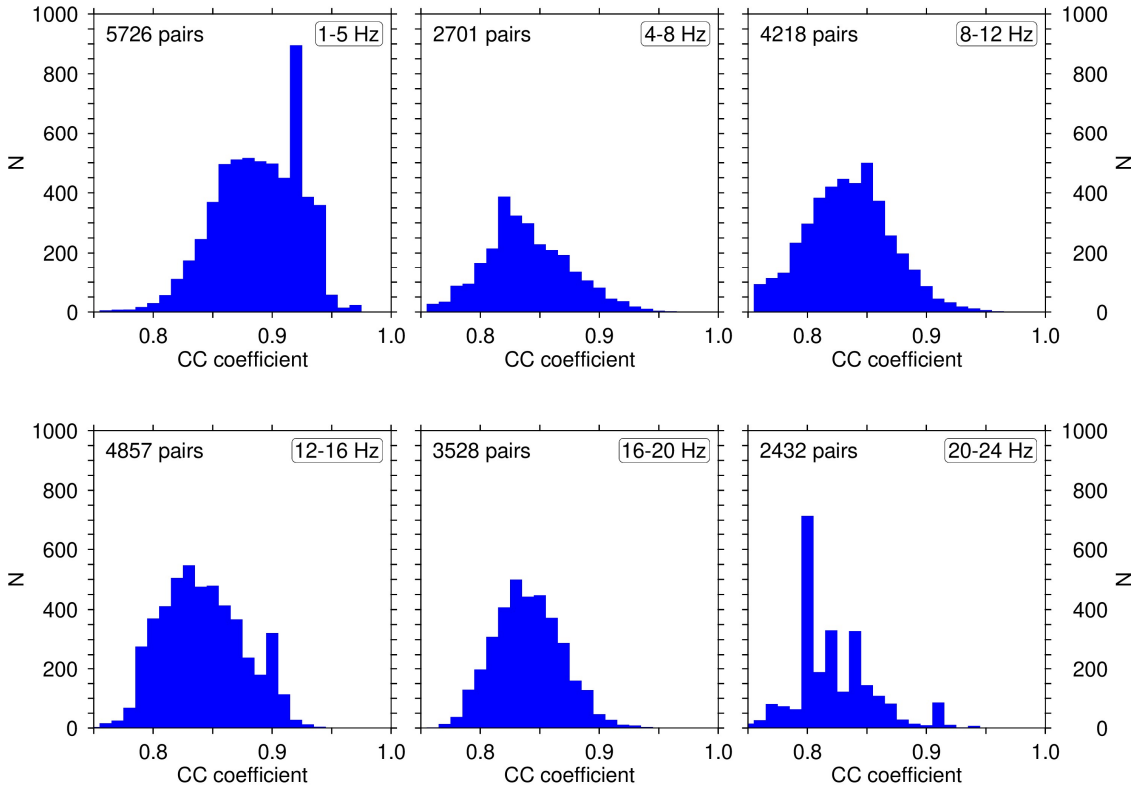

Figure S4. Histograms showing the distribution of cross-correlation coefficients achieved for different bandpass filters applied to the data. All six tests were performed on a subset of 140 events from swarm #1. For the later cross-correlation of all events in the dataset we used a bandpass filter of 1-5 Hz, which returned best test results.

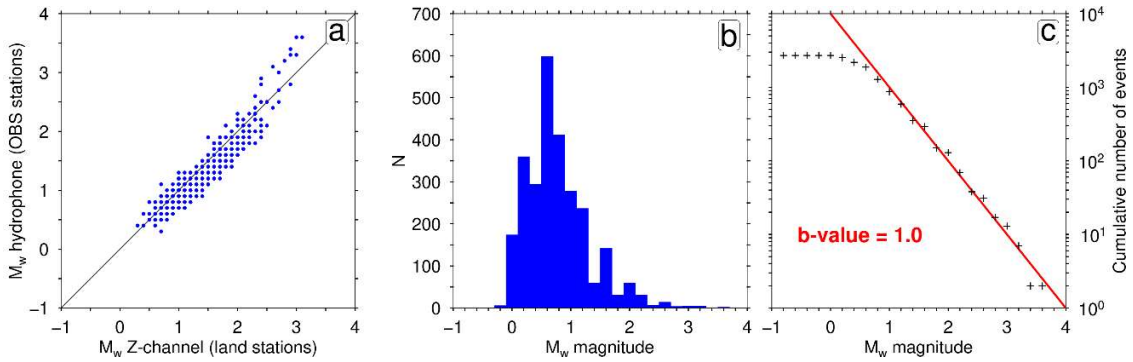

Figure S5. a) Comparison of Mw magnitudes computed from OBS hydrophone records and Mw magnitudes computed from the Z-channel of land stations. Note, only events are included where both values are available. b) Histogram of computed Mw magnitudes for the entire catalog. Note, the average value was used wherever both are available (hydrophone derived Mw and Z-channel derived Mw). In case only one values was available, this one was chosen. c) Frequency magnitude distribution of the all earthquakes in our catalog. The magnitude of completeness is at Mw ~ 0.6, derived from the plot. The solid red line indicates the b-value of the dataset (1.0).

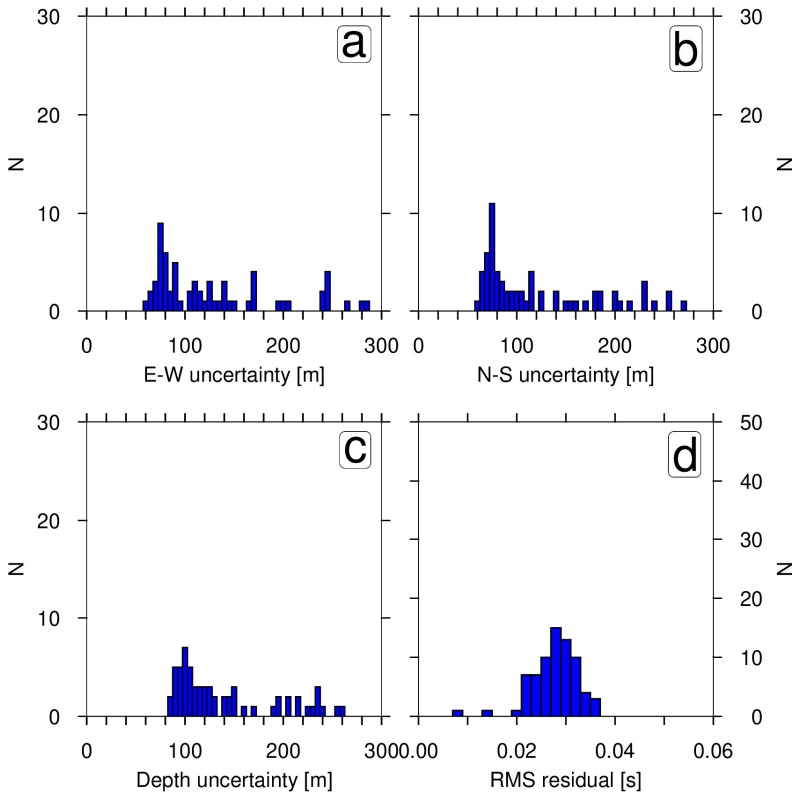

Figure S6. Relative location errors of HypoDD relocated hypocentres for swarm #1. Events were relocated with the singular-value-decomposition method, which applicable for small datasets only but produced more realistic location error estimates. Please note, that the spatial error represent relative uncertainties. a) Histogram of relative location uncertainty in E-W direction. b) Histogram of relative location uncertainty in N-S direction. c) Histogram of relative depth uncertainty. d) Histogram of traveltime residuals.

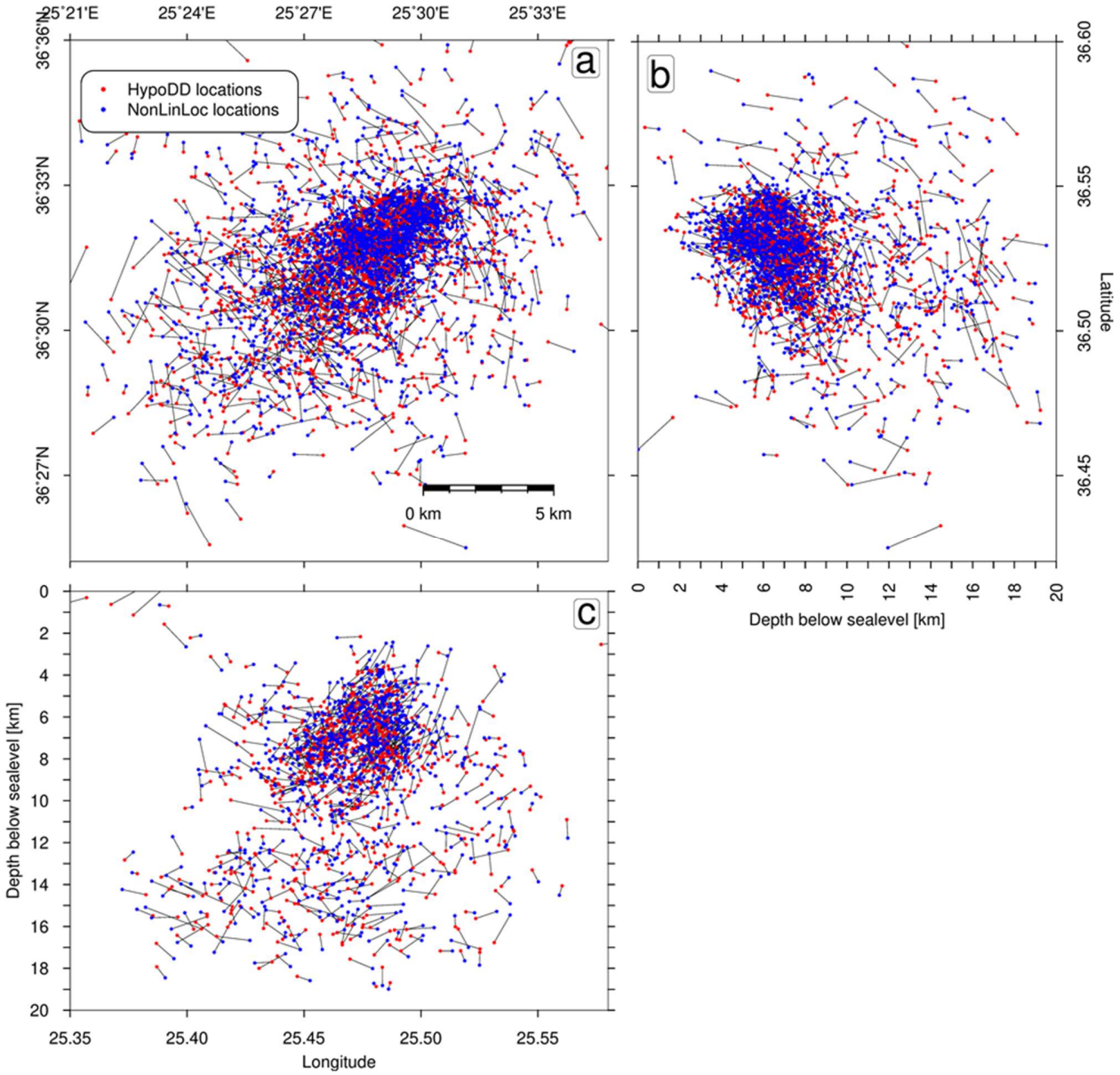

Figure S7. Illustration of the spatial differences between the location results of NonLinLoc and HypoDD for individual events. On average, the separation between the two hypocentres for individual events is 0.98 ± 0.54 km.

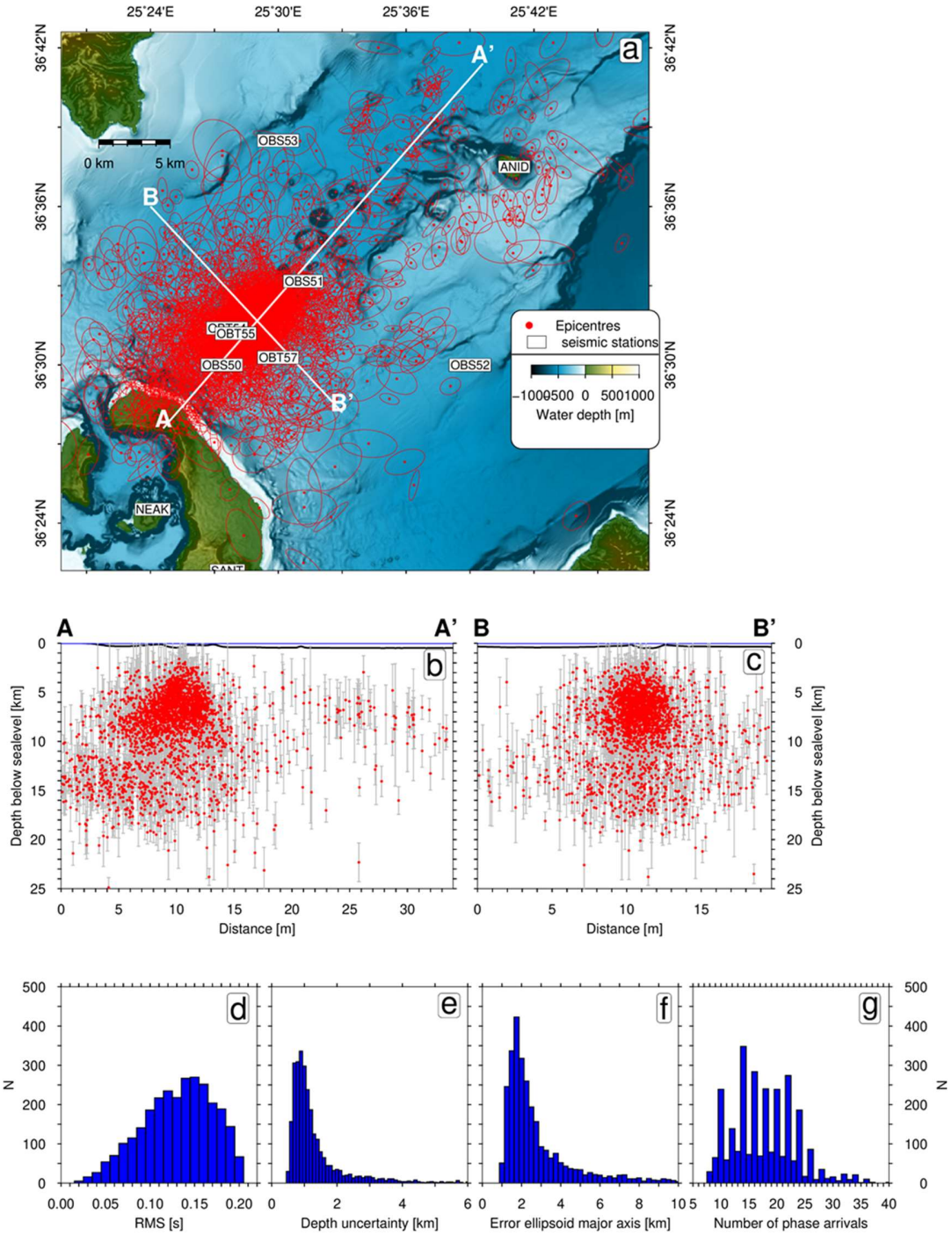

Figure S8. Representation of location errors for NonLinLoc located events. a) Individual epicentres together with 96% confidence error ellipses. Panels b and c show projected hypocentres along x-sections A-A‘ and B-B‘ with grey bars indicating the 96% confidence depth errors. d) Histogram of the root-mean-square errors (seconds) of the determined origin time. e) Histogram of depth errors. f) Histogram showing the length of the semi-major axis of the error ellipsoid. g) Histogram showing the numbers of phase arrivals used for location. Note, events with less than five phase arrivals have been omitted.

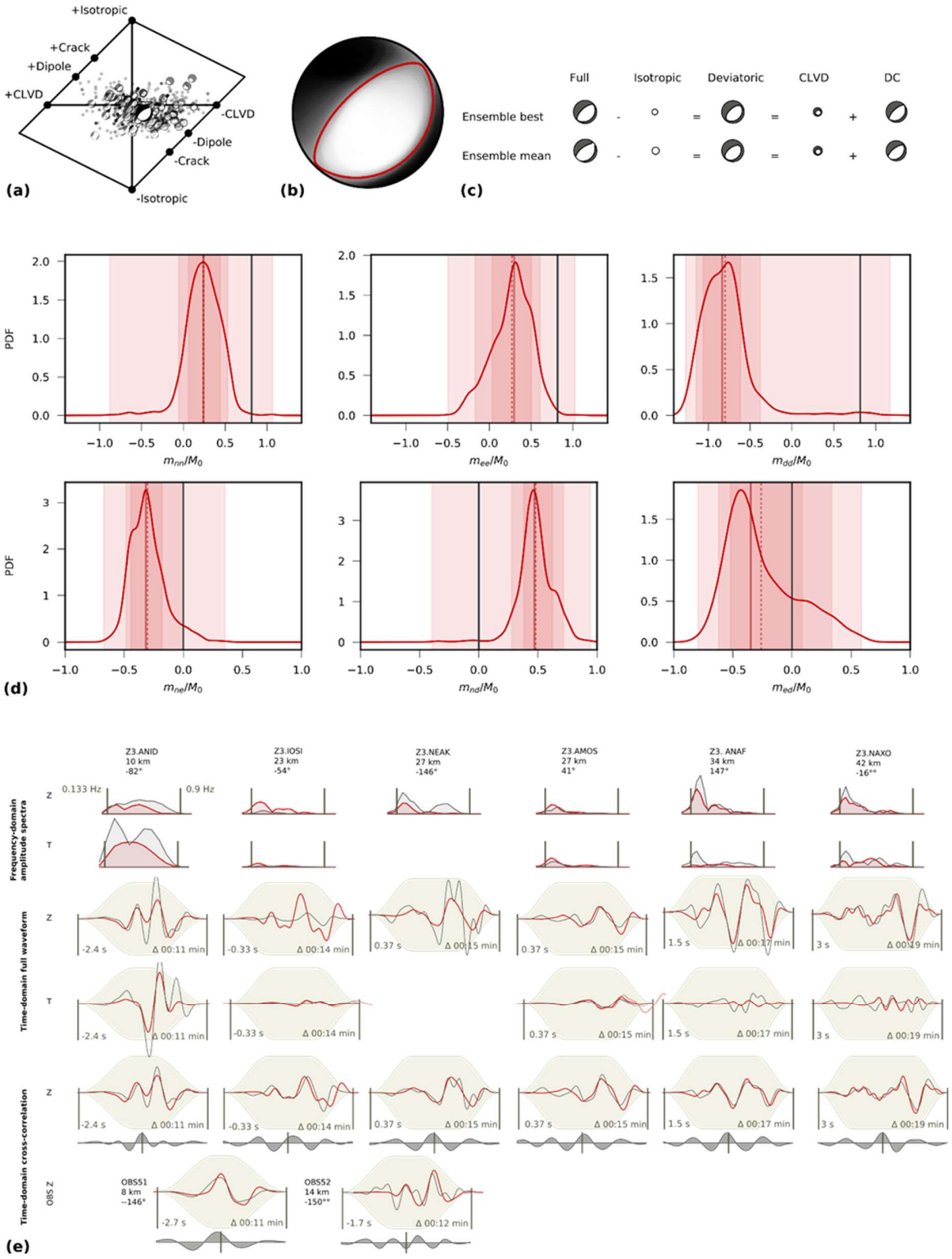

Figure S9. Moment tensor inversion result for event 2006-10-25 13:31. a) Bootstrap chain solutions in the Hudson plot. The largest focal mechanism corresponds to the solution with the smallest misfit. b) Fuzzy beachball, the overlain P radiation pattern of the bootstrap chain

solutions. The red line shows the best solution with respect to the misfit. c) Decomposition of the best full moment tensor solution and the mean solution of all bootstrap chains. d) The six graphs show the probability density functions of the relative contributions of the single moment tensor components. e) Misfits of synthetic (red) and observed (black) frequency domain amplitude spectra, time domain full waveforms and the cross-correlation based full-waveform fitting.

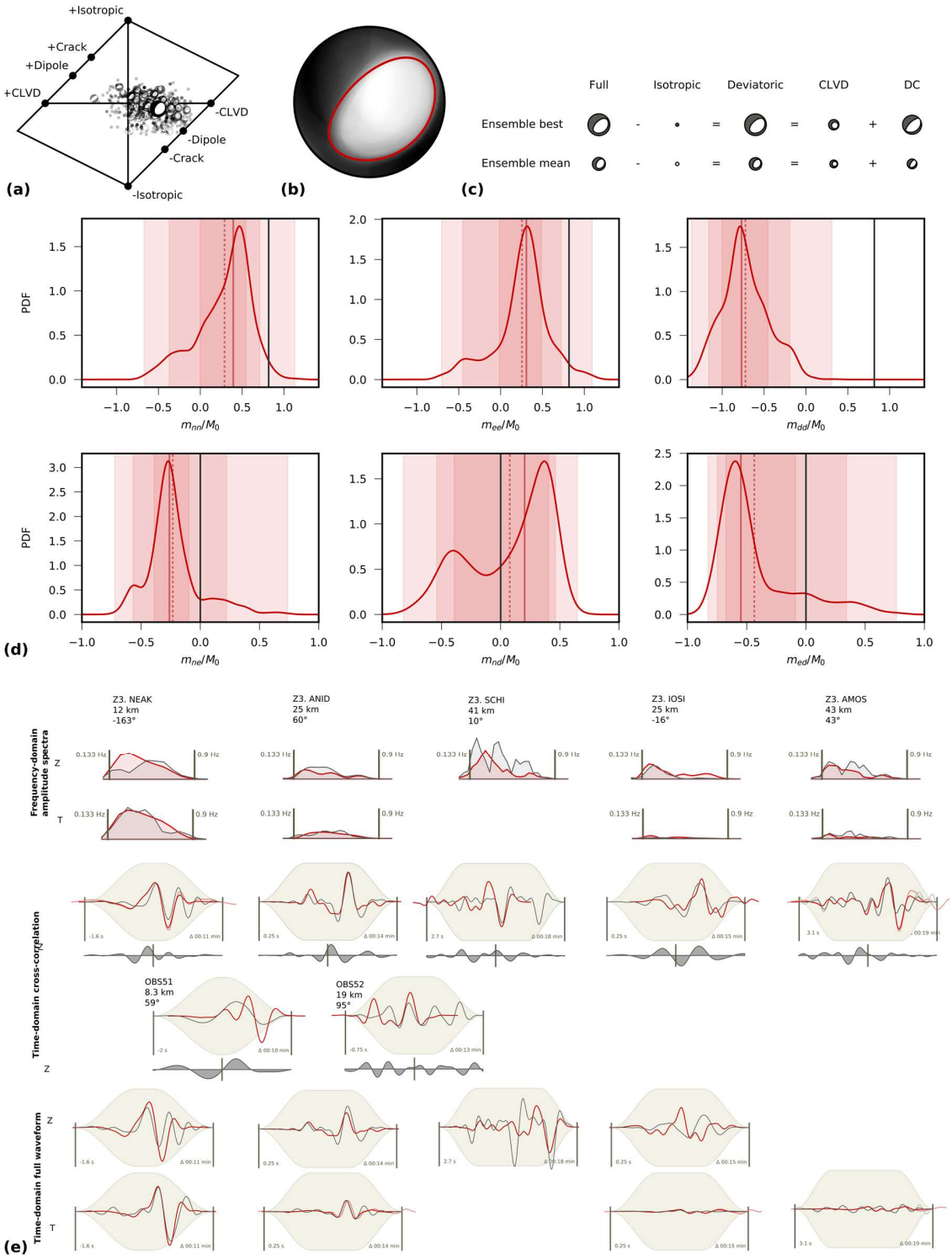

Figure S10. Moment tensor inversion result for event 2006-07-28 12:11. a) to e) as in Figure S9.

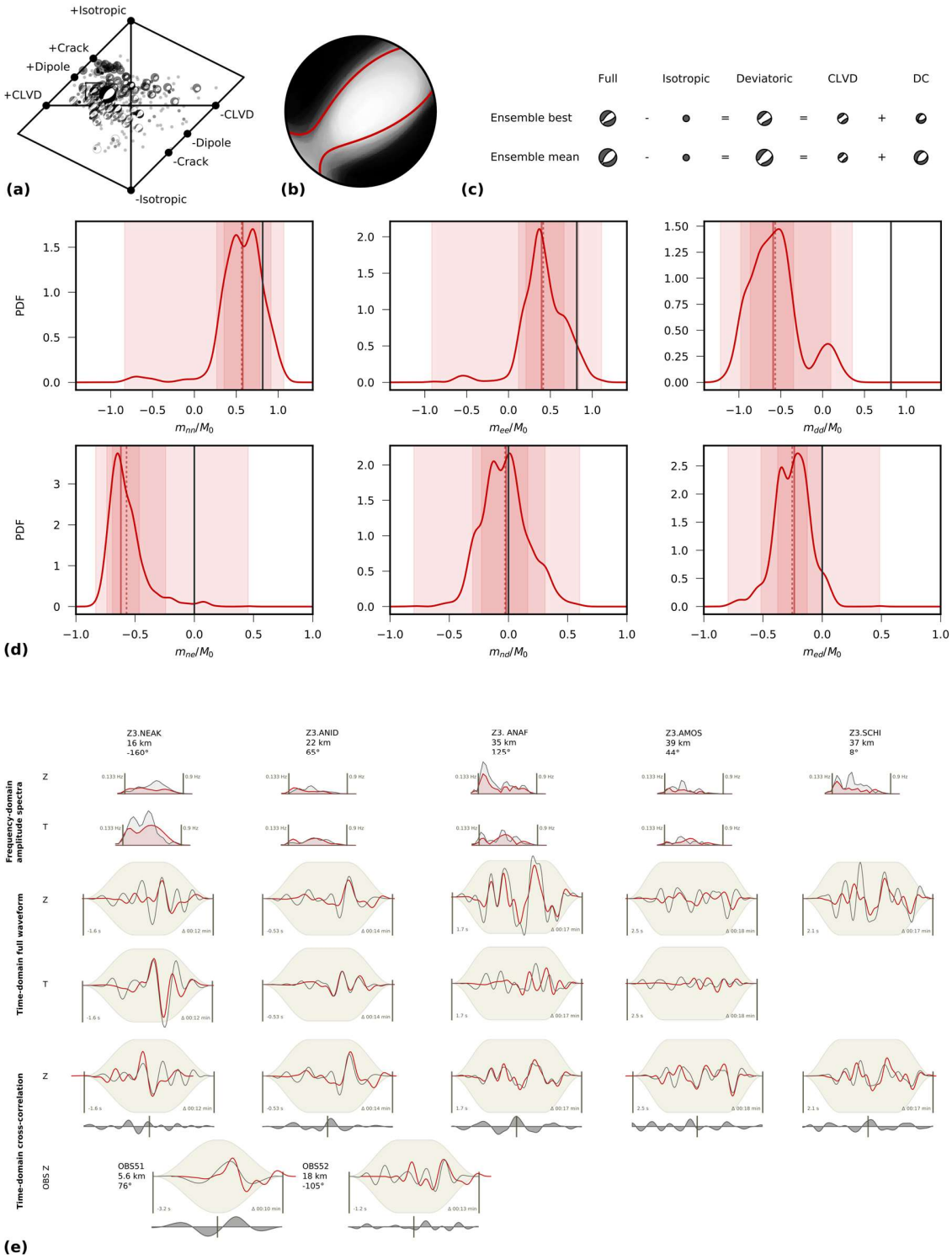

Figure S11. Moment tensor inversion result for event 2006-07-28 12:24. a) to e) as in Figure S9.

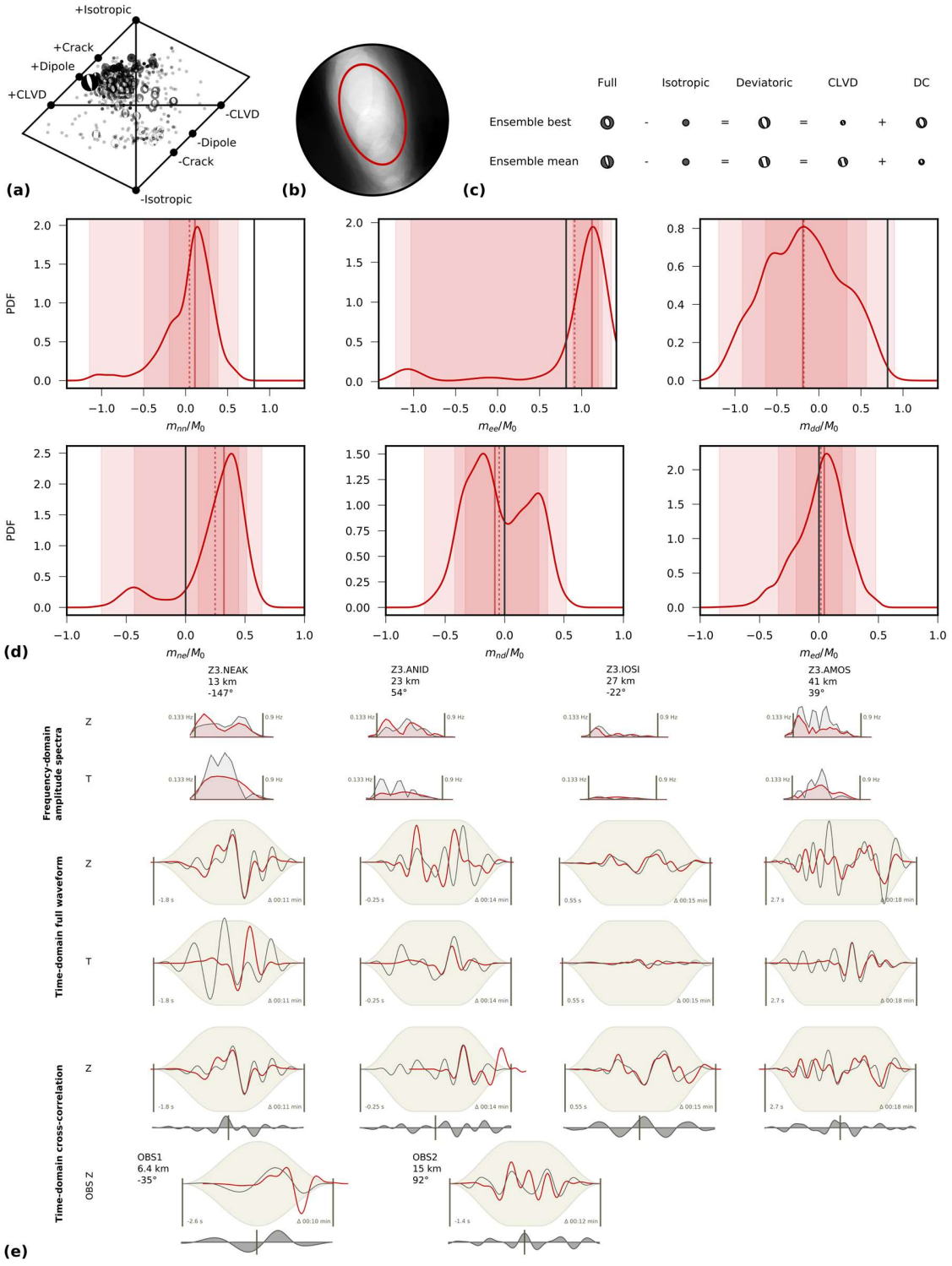

Figure S12. Moment tensor inversion result for event 2006-07-28 12:26. a) to e) as in Figure S9.

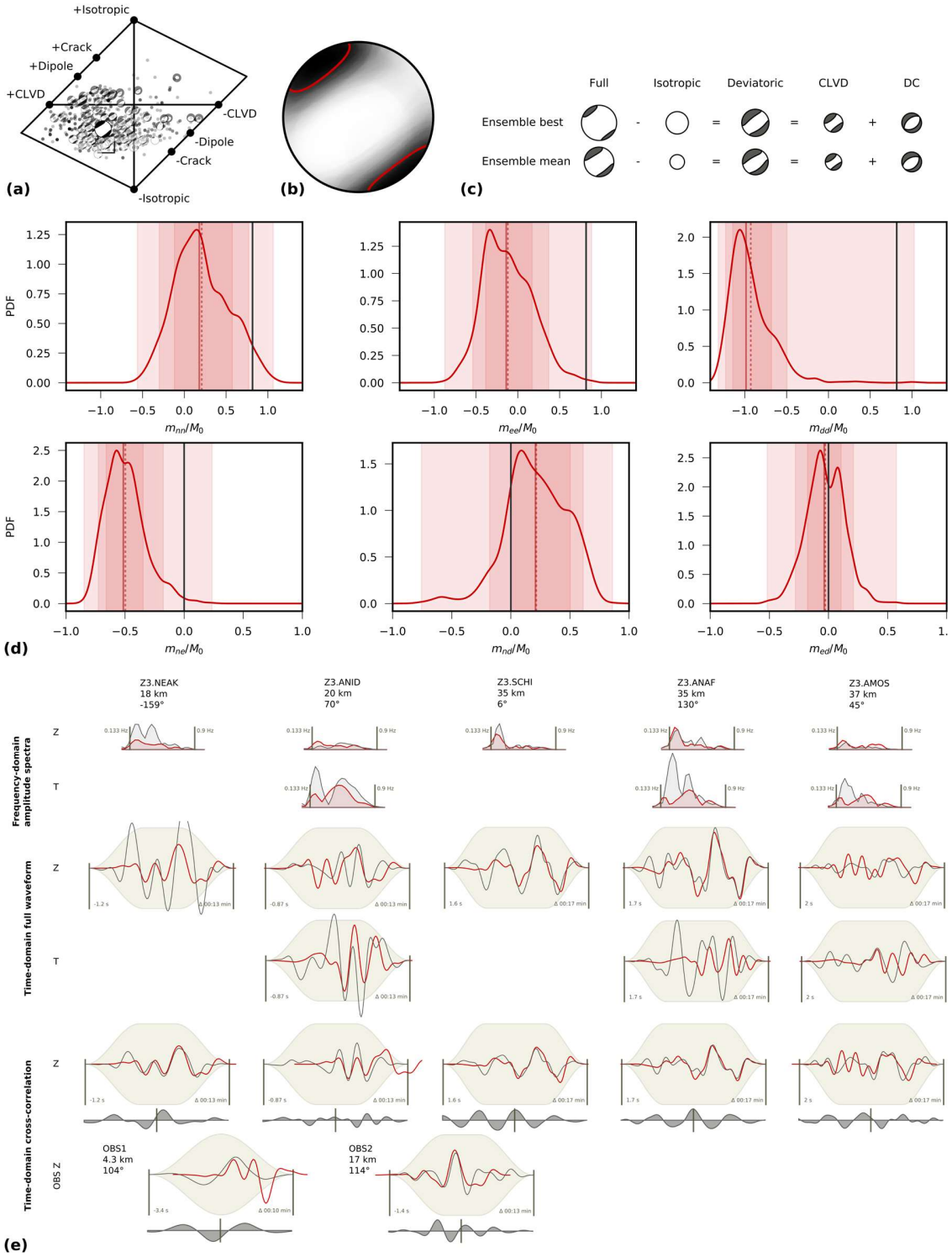

Figure S13. Moment tensor inversion result for event 2006-10-22 20:48. a) to e) as in Figure S9.

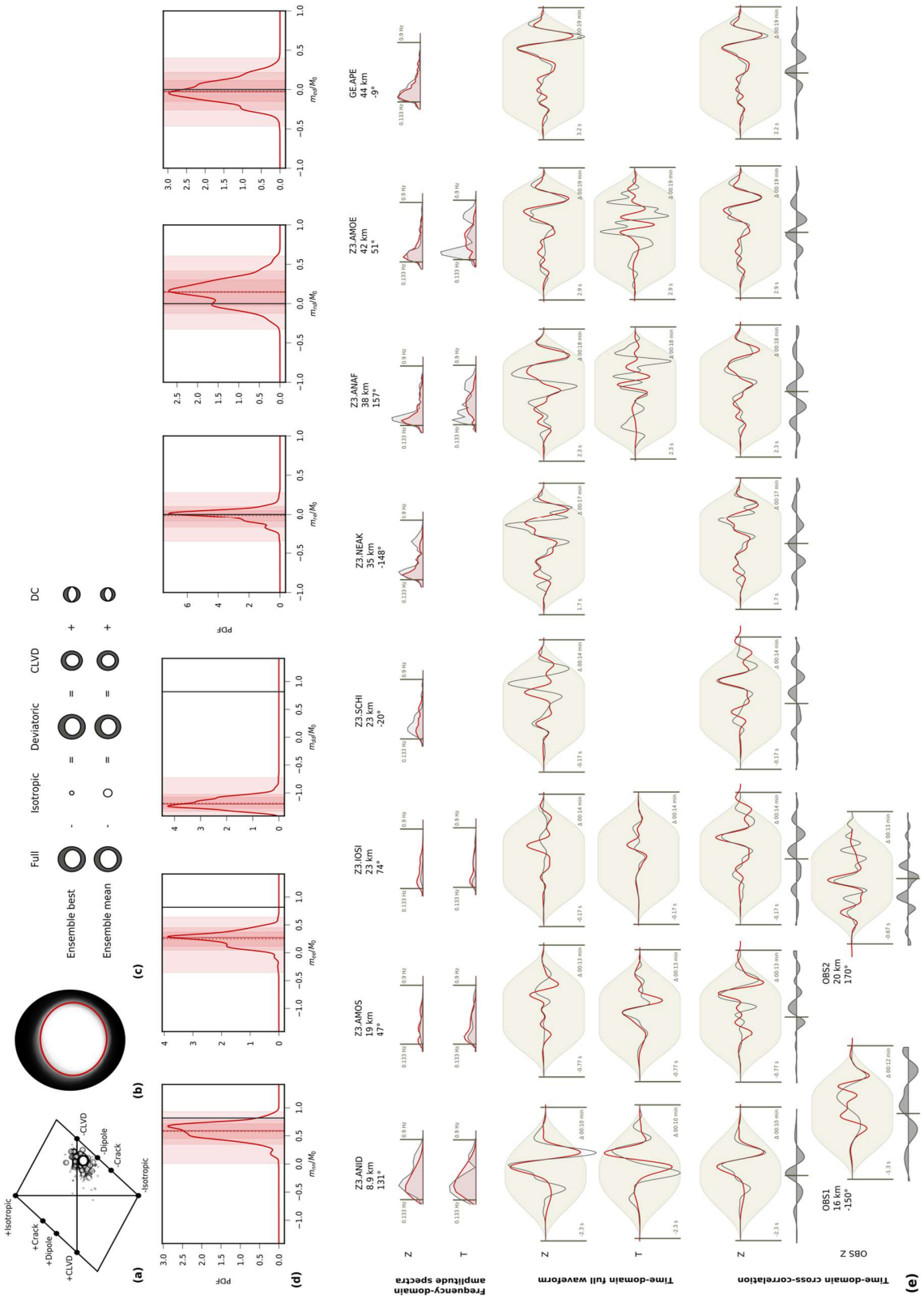

Figure S14. Moment tensor inversion result for event 2006-12-05 12:28. a) to e) as in Figure S9.

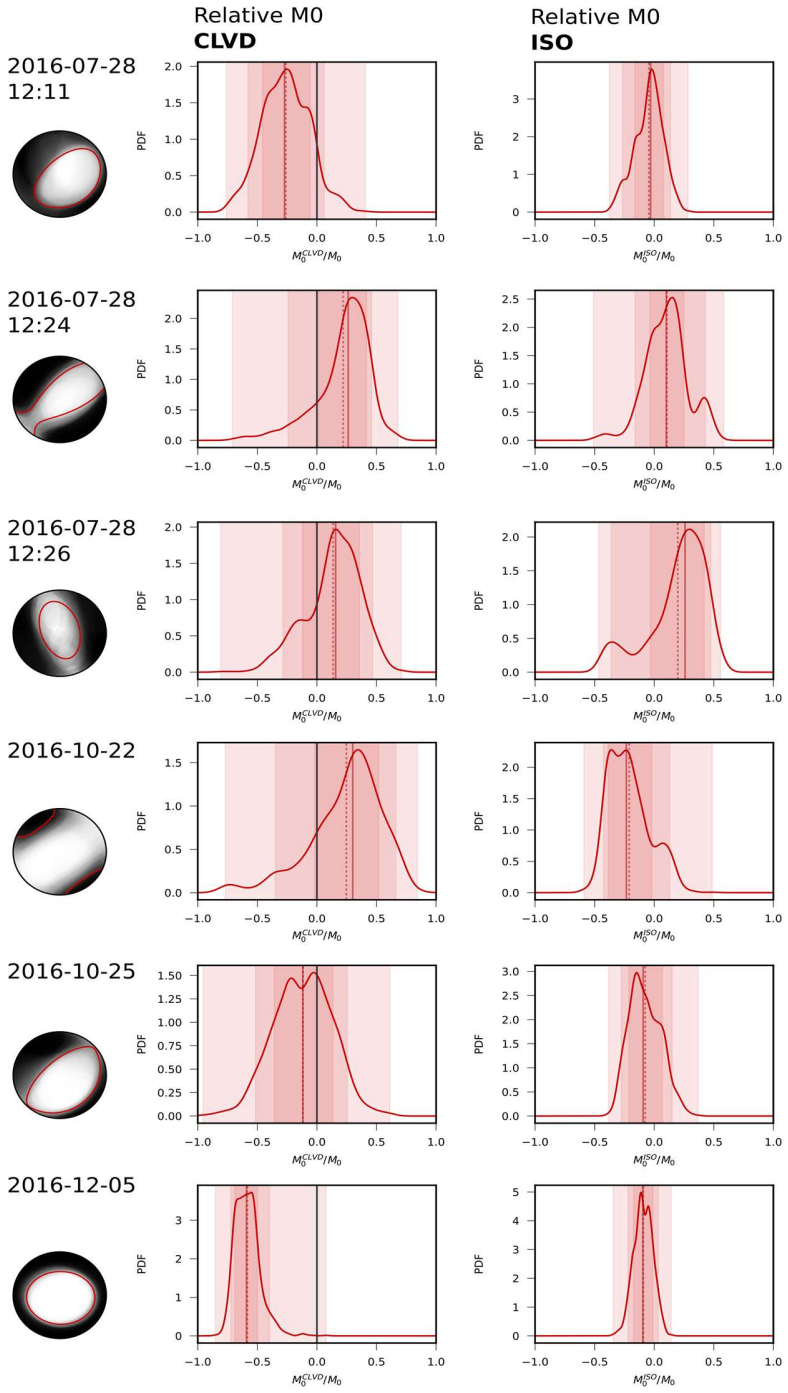

Figure S15. Relative contribution of non-Double Couple components to the seismic moment (M_0) of the six earthquakes. Each row corresponds to one event, showing, from left to right, the fuzzy MT with event date, the probability density distribution of the relative contribution of the CLVD component (M_0^{CLVD}/M_0) and the relative contribution of the isotropic component (M_0^{ISO}/M_0) as obtained from the bootstrap-chains. The overlapping red-shaded areas show the 68% and 90% confidence intervals and the minimum and maximum values (widest area). Peaked distributions indicate well resolved model parameters.